Applied Computational Electromagnetics Society

Express Journal

July 2016 Vol. 1 No. 7

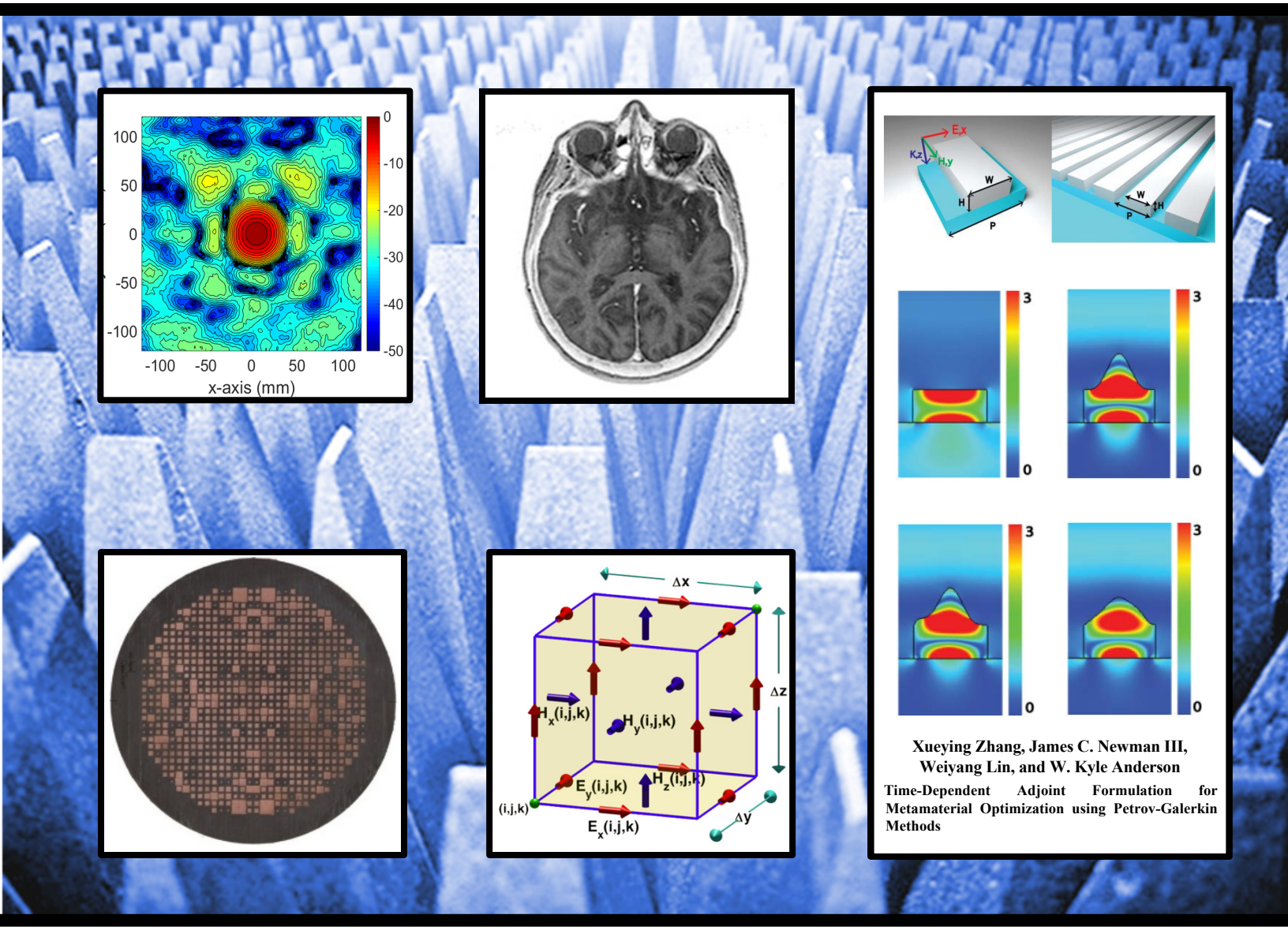

Xueying Zhang, James C. Newman III, Weiyang Lin, and W. Kyle Anderson

Time-Dependent Adjoint Formulation for Metamaterial Optimization using Petrov-Galerkin Methods

APPLIED COMPUTATIONAL ELECTROMAGNETICS SOCIETY EXPRESS JOURNAL

http://aces-society.org

GENERAL INFORMATION

PURPOSE AND SCOPE: The Applied Computational Electromagnetics Society ***(ACES) Express*** Journal hereinafter known as the ***ACES Express Journal*** is devoted to the timely and rapid exchange of information in computational electromagnetics, to the advancement of the state-of-the art, and the promotion of related technical activities. The primary objective of the information exchange is to inform the scientific community in a short amount of time on the developments of recent computational electromagnetics tools and their use in electrical engineering, physics, or related areas. The technical activities promoted by this publication include code validation, performance analysis, and input/output standardization; code or technique optimization and error minimization; innovations in solution technique or in data input/output; identification of new applications for electromagnetics modeling codes and techniques; integration of computational electromagnetics techniques with new computer architectures; and correlation of computational parameters with physical mechanisms.

SUBMISSIONS: The ***ACES Express Journal*** welcomes original, previously unpublished papers, relating to applied computational electromagnetics. Typical papers will represent the computational electromagnetics aspects of research in electrical engineering, physics, or related disciplines as well as research in the field of applied computational electromagnetics.

Manuscripts are to be submitted through the upload system of ***ACES*** web site http://aces-society.org Please see "Information for Authors" on inside of back cover and at ***ACES*** web site. For additional information contact the Editor-in-Chief:

Dr. Ozlem Kilic
Department of Electrical Engineering and Computer Science
The Catholic University of America
Washington, DC 20064
Email: kilic@cua.edu

SUBSCRIPTIONS: All members of the Applied Computational Electromagnetics Society are entitled to access and download the ***ACES Express Journal*** of any published journal article available at http://aces-society.org. ***ACES Express Journal*** is an online journal and printed copies are not available. Subscription to ACES is through the web site.

LIABILITY. Neither ***ACES***, nor the ***ACES Express Journal*** editors, are responsible for any consequence of misinformation or claims, express or implied, in any published material in an ***ACES Express Journal*** issue. This also applies to advertising, for which only camera-ready copies are accepted. Authors are responsible for all information contained in their papers. If any material submitted for publication includes material which has already been published elsewhere, it is the author's responsibility to obtain written permission to reproduce such material.

THE APPLIED COMPUTATIONAL ELECTROMAGNETICS SOCIETY EXPRESS JOURNAL

Vol. 1 No. 7 July 2016

TABLE OF CONTENTS

Non-uniform Surface Impedance Absorbing Boundary Condition for FDTD Method

Yunlong Mao [1], Atef Z. Elsherbeni [2], Si Li [1], and Tao Jiang [1]

[1] Department of Information and Communication Engineering
Harbin Engineering University, Harbin, Heilongjiang, 150001, China
maoyunlong@hrbeu.edu.cn, lisiharbin@hrbeu.edu.cn, jiangtao@hrbeu.edu.cn

[2] Department of Electrical and Computer Engineering
Colorado School of Mines, Golden, CO, 80401, USA
aelsherb@mines.edu

Abstract ─ Recently, we reported a novel absorbing boundary condition (ABC), surface impedance absorbing boundary (SIABC). SIABC has a comparable absorbing performance compared to CPML, but requires a sufficient long distance between the boundary and the scatter. In this paper, we focus on this issue and introduce the non-uniform SIABC. Non-uniform SIABC archives a similar absorbing performance as the uniform SIABC at a same distance, while the number of the air buffer cells is much smaller. Therefore, it is possible for us to make it more efficient relative to uniform SIABC or CPML. An example of a patch antenna is discussed to explore the accuracy and efficiency of non-uniform SIABC. We also compare the memory usage for uniform SIABC, non-uniform SIABC, and 10-layers CPML. All the results indicate that non-uniform SIABC requires much less memory, needs much less time for simulations, which makes it a potential of being one of the most popular ABCs in FDTD method.

Index Terms ─ CPML, FDTD, Non-uniform, SIABC.

I. INTRODUCTION

Surface impedance absorbing boundary condition is first introduced by us in [1]. SIABC comes from the concept of surface impedance boundary condition (SIBC) proposed by Leontovich in 1940s [2]. It is implemented by setting the impedance the same as free space. Compared to CPML [3], SIABC is extremely easy for understanding and for programming, meanwhile, it has a comparable absorbing performance relative to 10 layers CPML. Despite of these advantages, the disadvantage of SIABC is also obvious. In order to absorb the incident waves efficiently, a sufficient long distance between SIABC and the scatter is always required. Therefore, the memory requirement enlarges with the increase of number of air buffer cells. In some situations, this increase may be significant.

On the purpose of reducing the memory usage, we propose the non-uniform SIABC. Non-uniform gridding is a good way to reduce the simulation time with an acceptable accuracy. Non-uniform gridding is proposed originally to deal with complex geometrically details by changing large grids into smaller grids. However, for non-uniform SIABC, the general purpose of non-uniform gridding is inverted. We build larger grids for the air buffer between the boundaries and the scattering objects, in order to reduce the number of air buffer cells. There are a few non-uniform methods proposed [4-6], and in this paper, we will apply the gradually changing grid method as described in [7].

In the first section of this paper, we briefly described non-uniform sub-gridding and how it is combined with SIABC method. Later, we test the accuracy and efficiency of non-uniform SIABC with a mircostrip antenna example. The results are compared with 8-layers CPML and show a good agreement. The memory requirements are also compared to 10-layers CPML for general simulations. It can be concluded that non-uniform SIABC is an excellent ABC, and has the potential of being one of the most popular ABCs in FDTD method.

II. NON-UNIFORM FORMATTING

The geometrical illustration of grid discretization of non-uniform grid SIABC is displayed in Fig. 1 [7].

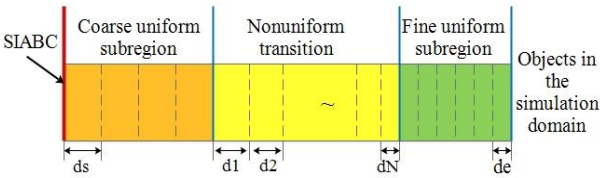

Fig. 1. Geometrical illustration of non-uniform SIABC.

Submitted On: June 18, 2016
Accepted On: July 26, 2016

In Fig. 1, the air buffer between the SIABC boundary and the objects inside the simulation domain is divided into 3 sub-regions: coarse uniform sub-region, non-uniform transition sub-region, and fine uniform sub-region. The objects in the simulation domain are located in the fine uniform sub-region. In the coarse uniform sub-region, the cell size is ds; in the non-uniform transition sub-region, the cell size changes from ds to de gradually with the same decreasing ratio, and in the fine uniform sub-region, the cell size is de. The length of the first cell in the transition sub-region is set as:

$$d1 = Rds, \tag{1}$$

where R is the ratio of change between subsequent half cells. In the transition sub-region, the length of each cell is changing gradually, hence, the length of each cell in the transition sub-region can be represented as:

$$dM = R^M ds, \tag{2}$$

where M is the index of the Mth cell in the transition sub-region. At the beginning of the fine uniform sub-region, the length of the fine cells should be:

$$de = R^{N+1} ds, \tag{3}$$

where N is the number of the cells in the transition sub-region. If the transition is desired to happen on a given length ΔT, the total length of the transition sub-region, in addition to one cell at both ends from the uniform regions is:

$$\Delta T + ds + de = \sum_{k=0}^{N+1} dsR^k = \frac{ds - deR}{1 - R}. \tag{4}$$

Therefore, ratio R can be calculated as:

$$R = \frac{\Delta T + de}{\Delta T + ds}. \tag{5}$$

Then, the number of cells, N, can be determined using:

$$N = \frac{\log(\mathrm{de}/\mathrm{ds})}{\log(\mathrm{R})} - 1. \tag{6}$$

One should notice that N must be an integer number. It can be rounded to its closest appropriate integer. A smoother transition can be archived if the transition sub-region is selected to be appropriately long.

Another important thing is that the size of the coarse grid should be chosen properly. As is known to all, the larger the coarse grid is, the smaller number of air buffer cells there will be. However, larger grid will cause instability during the simulation [8-10]. Therefore, a proper selection of coarse grids will reduce the cells needed meanwhile keep the stability of the simulation. As time duration is determined by the fine grids, there is no need to consider it separately.

The format of updating equations for non-uniform SIABC are totally the same as those of uniform SIABC method, while the cell size, dx, dy and dz, should be replaced with coarse grids.

III. VERIFICATION EXAMPLES

A. Microstrip patch antenna

In this example, a patch antenna as described in [7] is used to examine the performance of non-uniform SIABC. A microstrip rectangular patch antenna is constructed, as shown in Fig. 2. The problem domain is identified with grid size Δx=2 mm, Δy=2 mm, Δz=0.95 mm, which are regarded as fine grids in this example. A rectangular brick represents the substrate of the antenna with $60mm \times 40mm \times 1.9mm$ dimension and 2.2 dielectric constant. A PEC plate for the ground of the antenna is placed at the bottom side of the substrate covering its entire surface area. A PEC patch is centered on the top surface of the substrate with 56 mm width and 20 mm length in the x and y directions, respectively. The feeding point to the top patch is at the center of the long edge of the patch. A voltage source with 50 internal resistance between the ground plane and the feeding point is defined. This patch antenna operates at 3.45 GHz. The simulation with 8-layers CPML, uniform SIABC and non-uniform SIABC are employed in turn. In each simulation, the number of time steps is 8000. These simulations are executed on a personal computer operating with Inter(R) Core(TM) i7-4700MQ, running at 2.4 GHz.

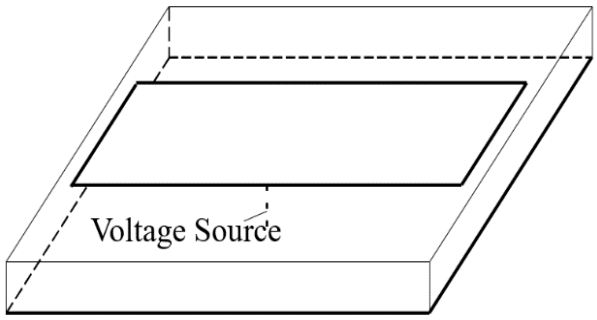

Fig. 2. A microstrip patch antenna configuration.

The performance of non-uniform SIABC is compared to uniform SIABC and 8-layers CPML. For the CPML case, the number of air buffer cells is 10. For the uniform SIABC case, the number of air buffer cells is 20. For the non-uniform SIABC cases, the number of air buffer is 20 and 30. The coarse grid is 5 mm in x and y directions, and 2.85 mm in z direction. The transition length is 21 mm in x and y directions and 8.55 mm in z direction. There are 2 fine grids before the transition region starts. A domain size comparison (in terms of number of cells) of 8-layers CPML, uniform SIABC, and non-uniform SIABC is shown in Table 1 along with the required CPU time. The comparison of the power reflection coefficient is shown in Fig. 3.

Table 1: Comparison of CPML, uniform SIABC and non-uniform SIABC in dimension size and simulation time

ABCs	nx×ny×nz	Domain Size	CPU Time (m)
CPML-8	66×56×38	140,448	8.01
SIABC-uniform	70×60×42	176,400	7.98
SIABC-non 20	52×42×22	48,048	1.35
SIABC-non 30	60×50×26	78,000	2.22

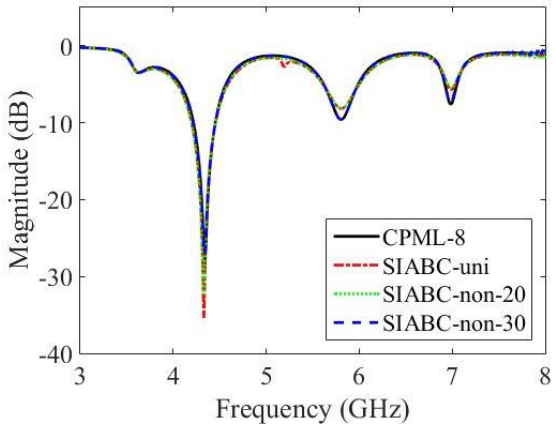

Fig. 3. Comparison of 8-layers CPML, uniform SIABC and non-uniform SIABC for power reflection coefficient.

From Table 1 and Fig, 3, one can figure out that compared to uniform SIABC or 8-layers CPML, non-uniform SIABC requires much less memory storage, and needs much less time for the simulation with the same reflection coefficient performance. For this example, the domain size for non-uniform SIABC is almost half of that for 8-layers CPML, while the time needed for the simulation is just around 1 fourth. That is because from the complexity aspect, SIABC is much easier than CPML.

B. Memory comparison

In this section, we compare the memory storage requirement for 10-layers CPML, uniform SIABC with its number of air buffer cells ranging from 20 to 50, and non-uniform SIABC with the same air buffer length as uniform SIABC has. Due to the fact that for non-uniform SIABC, the coarse grids will vary with different problems, we made an assumption that for all situations, the coarse grid is three times of the fine grid, and the transition length between coarse sub-region and fine sub-region is 3 times of a coarse grid. Also, there are 2 fine grids in front of the scattering object. Therefore, ratio R can be calculated as:

$$R = \frac{\Delta T + de}{\Delta T + ds} = \frac{9ds + ds}{9ds + 3ds} = \frac{5}{6}, \tag{7}$$

and the number of cells in the transition sub-region, N, should be:

$$N = \frac{\log(de/ds)}{\log(R)} - 1 = 5.0. \tag{8}$$

The air buffer gridding is illustrated in Fig. 4. There are 20 fine grids for uniform SIABC case and correspondingly, there are 10 cells for non-uniform SIABC case. There are 3 coarse grids and 2 fine grids. The other 5 cells comes from the transition sub-region, with their cell size decreasing from ds to de.

In order to reduce the number of cells for a certain length, the number of coarse grids should be as many as possible. In our discussion, as the number for fine grids is settled down, we should adjust the length of transition sub-region to ensure that we can have as many coarse grids as possible. Table 2 shows the number of air buffer cells comparison for uniform SIABC and non-uniform SIABC. In the first column, we list the number of air buffer cells for uniform SIABC, which is changing from 20 to 50. The rest of the columns list the corresponding number of cells for non-uniform SIABC: the number of course cells, the length for transition length in terms of de, the number of cells for the transition sub-region, N, the number of cells in the fine region, and the total number of cells used.

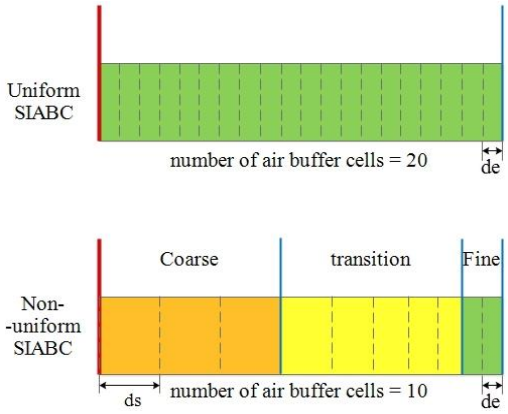

Fig. 4. Air buffer cells configurations for uniform SIABC and non-uniform SIABC with fixed air buffer length.

Table 2: Number of air buffer cells comparison

Uniform (cells)	Non-uniform (cells)				
	Coarse	Transition Length (de)	N	Fine	Total
20	3	9	5	2	10
30	6	10	6	2	14
40	9	11	6	2	17
50	13	9	5	2	21

The memory comparison result is shown in Fig. 5. Generally speaking, by using non-uniform SIABC, the memory requirement is significantly smaller than 10-

layers CPML, especially for problems with small domain size.

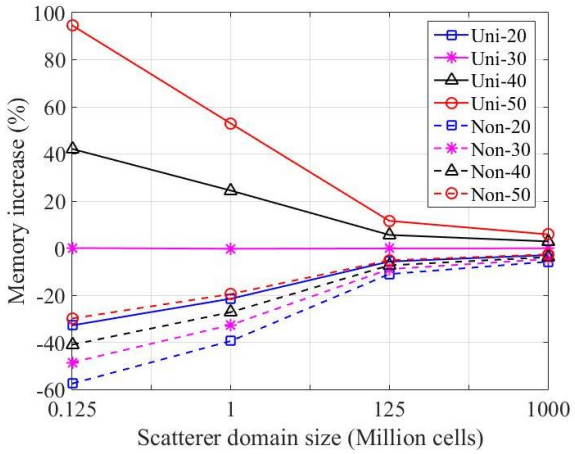

Fig. 5. Memory increase relative to 10-layers CPML.

IV. CONCLUSION

In this paper, an advanced absorbing boundary condition, non-uniform SIABC is proposed which is a combination of non-uniform grid and SIABC. By applying non-uniform grid, we significantly reduced the number of air buffer cells between the SIABC boundaries and the scattering objects leading to much smaller memory requirements relative to uniform SIABC or CPML with acceptable accuracy. Hence, non-uniform SIABC has the potential of being one of the most easy to implement with good performance and less memory requirements ABC for electromagnetic simulations.

REFERENCES

[1] Y. Mao, A. Z. Elsherbeni, S. Li, and T. Jiang, "Surface impedance absorbing boundary for terminating FDTD simulations," *Applied Computational Electromagnetics Society Journal*, vol. 29, pp. 1035-1046, 2014.

[2] M. Leontovich, "Approximate boundary conditions for the electromagnetic field on the surface of a good conductor," *Investigations on Radiowave Propagation*, vol. 2, pp. 5-12, 1948.

[3] J. A. Roden and S. D. Gedney, "Convolutional PML (CPML): An efficient FDTD implementation of the CFS-PML for arbitrary media," *Microwave and Optical Technology Letters*, vol. 27, pp. 334-338, 2000.

[4] S. S. Zivanovic, K. S. Yee, and K. K. Mei, "A subgridding method for the time-domain finite-difference method to solve Maxwell's equations," *Microwave Theory and Techniques, IEEE Transactions on*, vol. 39, pp. 471-479, 1991.

[5] P. Thoma and T. Weiland, "A consistent subgridding scheme for the finite difference time domain method," *International Journal of Numerical Modelling: Electronic Networks, Devices and Fields*, vol. 9, pp. 359-374, 1996.

[6] K. Xiao, D. J. Pommerenke, and J. L. Drewniak, "A three-dimensional FDTD subgridding algorithm with separated temporal and spatial interfaces and related stability analysis," *IEEE Transactions on Antennas & Propagation*, vol. 55, pp. 1981-1990, 2007.

[7] A. Z. Elsherbeni and V. Demir, *The Finite-difference Time-domain Method for Electromagnetics with MATLAB® Simulations*. 2nd ed., Edison, NJ: SciTech Publishing, an Imprint of the IET, 2016.

[8] J. S. Juntunen and T. D. Tsiboukis, "Reduction of numerical dispersion in FDTD method through artificial anisotropy," *IEEE Transactions on Microwave Theory & Techniques*, vol. 48, pp. 582-588, 2000.

[9] T. Martin and L. Pettersson, "Dispersion compensation for Huygens' sources and far-zone transformation in FDTD," *IEEE Transactions on Antennas & Propagation*, vol. 48, pp. 494-501, 2000.

[10] J. B. Schneider and R. J. Kruhlak, "Dispersion of homogeneous and inhomogeneous waves in the Yee finite-difference time-domain grid," *IEEE Transactions on Microwave Theory & Techniques*, vol. 49, pp. 280-287, 2001.

[11] J. H. Beggs, R. J. Luebbers, K. S. Yee, and K. S. Kunz, "Finite-difference time-domain implementation of surface impedance boundary conditions," *Antennas and Propagation, IEEE Transactions on*, vol. 40, pp. 49-56, 1992.

Time-Dependent Adjoint Formulation for Metamaterial Optimization using Petrov-Galerkin Methods

Xueying Zhang, James C. Newman III, Weiyang Lin, and W. Kyle Anderson

Simcenter: Center of Excellence in Applied Computational Science and Engineering
University of Tennessee, Chattanooga, TN 37403, USA
Xueying-Zhang@mocs.utc.edu, James-Newman@utc.edu, Weiyang-Lin@mocs.utc.edu, Kyle-Anderson@utc.edu

Abstract ─ A time-dependent discrete adjoint algorithm for electromagnetic problems is presented. The governing equations are discretized with a semi-discrete Petrov-Galerkin method. Time advancement is accomplished using an implicit, second-order backward differentiation formula (BDF2). An all-dielectric metamaterial is proposed and gradient-based shape design optimization is conducted. Hicks-Henne functions are utilized for shape parameterization to ensure smooth surfaces, and linear elasticity employed to adapt interior mesh points to boundary modifications. The cost function used in the design optimization attempts to widen the bandwidth of the metamaterial over a desired frequency range. Optimization results demonstrate an increase of the full width at half maximum (FWHM) of reflection from 111 THz to 303 THz.

Index Terms ─ Adjoint-based sensitivity analysis, design optimization, finite element method, metamaterial, Petrov-Galerkin.

I. INTRODUCTION

In recent years, the Petrove-Galerkin (PG) method has become a popular approach in solving a wide range of convection-dominated problems, such as computational fluid dynamics and electromagnetics [1, 2]. The primary benefits of using PG methods arise from their suitability for efficient parallel computing and their high performance of efficiency over DG methods [1]. Since sensitivity analysis is required for gradient-based optimization, the PG method has been extended to provide sensitivity derivatives for both steady-state and time-dependent problems.To this end, a discrete adjoint approach for time-dependent acoustic problems is described in [3, 4] for a Petrov-Galerkin method.

Metamaterials [5] are artificially structured materials with sub-wavelength scale building blocks. The optical properties of metamaterials depend on the constituent materials and geometries of the building blocks. The ability to design such metamaterials opens the pathway for creating materials with designer optical properties. Over the past decade, metamaterials have shown the ability of controlling light propagation [6], absorption and emission [7, 8]. The rapid development of metamaterial research has lead to many scientific breakthroughs such as negative refraction, invisible cloaking, and ultra-compact optical elements [5-9].

In this paper, the research described in [3, 10] is extended for optimization of metamaterials at optical frequencies. A time-dependent discrete adjoint method is employed to obtain sensitivity derivatives. An all-dielectric metamaterial is proposed and optimization is conducted. To follow, the governing equations and discretization method, the adjoint-based sensitivity analysis and shape optimization algorithm, and numerical results are presented.

II. GOVERNING EQUATIONS AND DISCRETIZATION METHOD

The governing equations considered are the two-dimensional source-free Maxwell's equations, which can be written in the conservative form:

$$\frac{\partial q(x,t)}{\partial t}+\frac{\partial F(q(x,t))}{\partial x}+\frac{\partial G(q(x,t))}{\partial y}=0, \tag{1}$$

where q, F and G are given by:

$$\begin{aligned} q &= \{D_x, D_y, B_z\}^T, \\ F &= \{0, B_z/\mu, D_y/\varepsilon\}^T, G \\ &= \{-B_z/\mu, 0, -D_x/\varepsilon\}^T, \end{aligned} \tag{2}$$

or

$$\begin{aligned} q &= \{B_x, B_y, D_z\}^T, \\ F &= \{0, -D_z/\varepsilon, -B_y/\mu\}^T, G \\ &= \{D_z/\varepsilon, 0, B_x/\mu\}^T, \end{aligned} \tag{3}$$

for a transverse-electric (TE) mode or a transverse-magnetic (TM) mode, respectively. In the equations above, μ and ε represent the relative permeability and permittivity, respectively. These parameters are assumed to be constants in the current work.

The Petrov-Galerkin discretization begins by formulating a weighted-integral statement of the governing equations by multiplying Eq. (1) by a set of weighting functions, and integrating within each element, as:

Submitted On: July 1, 2016
Accepted On: September 11, 2016

$$\int_{\Omega_k}[\phi]\left(\frac{\partial q}{\partial t}+\frac{\partial F}{\partial x}+\frac{\partial G}{\partial y}\right)d\Omega_k=0, \quad (4)$$

where ϕ is a weighting function defined by the Streamline Upwind/Petrov-Galerkn (SUPG) method given by:

$$[\phi]=N[I]+\left(\frac{\partial N}{\partial x}[A]+\frac{\partial N}{\partial y}[B]\right)[\tau] = N[I]+[P], \quad (5)$$

where $[\tau]$ represents the stabilization matrix and can be obtained using the following definitions:

$$[\tau]^{-1}=\sum_{k=1}^{n}\left|\frac{\partial N_k}{\partial x}[A]+\frac{\partial N_k}{\partial y}[B]\right|, \quad (6)$$

$$\left|\frac{\partial N_k}{\partial x}[A]+\frac{\partial N_k}{\partial y}[B]\right|=[T][|\Lambda|][T]^{-1}, \quad (7)$$

where $[T]$ and $[\Lambda]$ are the right eigenvectors and eigenvalues of the matrix on the left hand side of Eq. (7) respectively, and $[T]^{-1}$ represents the inverse of $[T]$.

Integrating Eq. (4) by parts, the weak formulation of the problem for each elementcan be written as:

$$\int_{\Omega_k}N_i\frac{\partial \boldsymbol{q}_p}{\partial t}d\Omega_k-\int_{\Omega_k}\left[\frac{\partial N_i}{\partial x}F(\boldsymbol{q}_p)+\frac{\partial N_i}{\partial y}G(\boldsymbol{q}_p)\right]d\Omega_k+\int_{\Omega_k}[P]\left[\frac{\partial \boldsymbol{q}_p}{\partial t}+\frac{\partial F(\boldsymbol{q}_p)}{\partial x}+\frac{\partial G(\boldsymbol{q}_p)}{\partial y}\right]d\Omega_k+\int_{\Gamma_k}N_iH(\boldsymbol{q}_p^+,\boldsymbol{q}_p^-,\boldsymbol{n})dS=0, \quad (8)$$

where the solution is approximated as $q_p=\sum_{i=1}^{M}\tilde{q}_{p_i}N_i(x)$. In Eq. (8), $H(q_p^+,q_p^-,n)$ represents the flux on the element boundaries, which is determined from the data on either side of the interface using a Riemann solver described in [1]. Equation (8) can be written as an ordinary differential equation in time, which is integrated using an implicit, second-order backward difference formula (BDF2).

III. ADJOINT-BASED UNSTEADY SHAPE OPTIMIZATION

In gradient-based optimization, sensitivity derivatives of the objective function are utilized to construct an appropriate search direction for improving the design. For the direct approach a linear system is formed and solved for each design variable. Numerical evaluation, such as central finite-difference, requires two high converged solutions for each design variable. When the number of design variables is greater than the number of objective functions, adjoint-based sensitivity analysis is the most efficient option for obtaining these derivatives. The number of linear systems requiring solution is equal to the number of objective functions.

A. Design variables and shape parametrization

During a design cycle, the geometry is modified through surface node displacements according to a defined parameterization. The specific method will dictate the set of geometric design variables. A number of surface parameterization methods have been utilized for this purpose in the literature, such as Bezier, B-spline, Hicks-Henne functions, basis vectors, free-form deformation, etc. In this paper, the Hicks-Henne sine bump function is utilized to ensure smooth surface shape, given by:

$$b_i(x_{si},\beta_m)=\beta_m sin^4\left(\pi x_{si}^{\ln(0.5)/\ln(x_{sm})}\right), \quad (9)$$

where the design variables are set to be the magnitudes of the bump functions $\boldsymbol{\beta}=\{\beta_m, m=1,\cdots,N_d\}$, where N_d represents the total number of design variables. In Eq. (9), b_i represents the surface node displacement at x_{si} due to the displacement of the surface node at x_{sm}, and β_m denotes the m^{th} component of the design variables associated with the surface node at x_{sm}. The modified surface coordinates are computed by:

$$x_{si}^{new}=x_{si}^{old}+\sum_{m=1}^{N_d}b_i(x_{si},\beta_m). \quad (10)$$

As the surface mesh deformation is obtained, the interior mesh points are deformed using linear elasticity to prevent the generation of overlapping elements. This system of equations may be expressed as $[K]\Delta x=\Delta x_s$, where $[K]$ represents the stiffness matrix as found in solid mechanics applications.

For gradient-based optimization the function I refers to a scalar-valued objective function used for minimization. A general formulation for the objective function is expressed in terms of the design variables as $I=I\left(X(\boldsymbol{\beta}),\tilde{\boldsymbol{q}}(X(\boldsymbol{\beta}))\right)$, where $\tilde{\boldsymbol{q}}$ represents the computed unsteady solution, X represents the computational mesh and $\boldsymbol{\beta}$ represents the set of design variables, which control the modification of the surface geometry.

B. Adjoint-base sensitivity calculation

The unsteady residual for time step n can be expressed as:

$$R^n(\boldsymbol{\beta},X,\tilde{\boldsymbol{q}}^n,\tilde{\boldsymbol{q}}^{n-1},\tilde{\boldsymbol{q}}^{n-2})=0. \quad (11)$$

The sensitivity derivative can be computed using a forward mode direct differentiation by examining the function dependencies of the objective function. The total differential of I with respect to β can be expressed as:

$$\frac{dI}{d\beta}=\frac{\partial I}{\partial X}\frac{\partial X}{\partial \beta}-\sum_{n=1}^{ncyc}\frac{\partial I}{\partial q^n}\left[\frac{\partial R^n}{\partial q^n}\right]^{-1}\left(\frac{\partial R^n}{\partial X}\frac{\partial X}{\partial \beta}+\frac{\partial R^n}{\partial q^{n-1}}\frac{\partial q^{n-1}}{\partial \beta}+\frac{\partial R^n}{\partial q^{n-2}}\frac{\partial q^{n-2}}{\partial \beta}\right). \quad (12)$$

The adjoint method eliminates the computational overhead caused by repetitive calculations of the solution sensitivities by transposing the inverse of the Jacobian matrix. While a detailed derivation of the procedure is given in [3], the total differential of the objective function may be expressed in terms of the adjoint vector as:

$$\frac{dI}{d\beta}=\frac{\partial I}{\partial X}\frac{\partial X}{\partial \beta}+\sum_{n=1}^{ncyc}\left(\left[\lambda_q^n\right]^T\left(\frac{\partial R^n}{\partial X}\frac{\partial X}{\partial \beta}\right)\right), \quad (13)$$

where

$$\lambda_q^n=-\left[\frac{\partial R^n}{\partial q^n}\right]^{-T}\left(\left[\frac{\partial I}{\partial q^n}\right]^T+[\psi_1^{n+1}]^T+[\psi_2^{n+2}]^T\right), \quad (14)$$

$$\psi_1^n = \left[\frac{\partial R^n}{\partial q^{n-1}}\right]^T \lambda_q^n, \psi_2^n = \left[\frac{\partial R^n}{\partial q^{n-2}}\right]^T \lambda_q^n, \quad (15)$$

are the adjoint variables.

C. Shape optimization algorithm

Once the sensitivity derivatives of the objective function are evaluated, they are utilized to predict an appropriate search direction. The basic algorithm can be written as:

Algorithm. A discrete adjoint formulation for time-dependent sensitivity derivatives:

(1) Set ψ_1^{n+1}, ψ_2^{n+1}, ψ_2^{n+2} to be zero. Set n to be ncyc.

(2) Solve Eq. (14) for the adjoint variable.

(3) Set the sensitivity derivatives by:

$$\frac{dI}{d\beta} = \frac{dI}{d\beta} + \frac{\partial I}{\partial X}\frac{\partial X}{\partial \beta} + \left[\lambda_q^n\right]^T \left(\frac{\partial R^n}{\partial X}\frac{\partial X}{\partial \beta}\right). \quad (16)$$

(4) Set $n = n - 1$.

(5) Set $\psi_2^{n+2} = \psi_2^{n+1}$, solve Eq. (15) for ψ_1^{n+1} and ψ_2^{n+1}.

(6) If $n = 1$, stop; otherwise go to step 2.

IV. NUMERICAL RESULTS

A. All-dielectric metamaterial and objective function

All-dielectric metamaterials offer a potential low-loss alternative to plasmonic metamaterials at optical frequencies [11]. In the current work, an all-dielectric metamaterial made of silicon on SiO_2 substrate is proposed as the initial design model. Figures 1 (a-b) illustrate the schematic of metamaterial unit cell and array. The silicon resonators with dimension of $W = 200$ nm and $H = 100$ nm are placed on top of a SiO_2 substrate (regarded infinite) with periodicity of $P = 300$nm. As shown the Fig. 1 (a), the metamaterial is illuminated with polarized light. The electric field is polarized along the x-direction and the magnetic field along the y-direction with wave vector k in z-direction. In this case, the light transmits from the air to the SiO_2 through the silicon resonators.

The metamaterial proposed above is modeled and simulated by an in-house code developed at the Simcenter. The results of reflection over frequency range of 350-650 THz are shown in Fig. 1 (c), with full width at half maximum (FWHM) of 111 THz (479~590 THz) in reflection. For comparative purposes, the current results are shown with those from the commercial software ANSYS© HFSS [12]. The reflection indicates that the metamaterial has the maximum reflection at 516 THz. The electric field distribution at 516 THz, depicted in Fig. 1 (d), clearly illustrates this reflection.

The objective of the current design optimization is to widen the bandwidth of the metamaterial. Accordingly, an objective function is proposed as:

$$I = \int_{f1}^{f2} (1 - Reflection)^2 \, df, \quad (17)$$

where f_1 and f_2 represent the lower and upper bound of the desired frequency range.

B. Optimization results

In the current research the DAKOTA toolkit [13] was utilized. DAKOTA's optimization capabilities include a wide variety of optimization methods, and an interface to link with third-party routines. The optimization is performed using a quasi-Newton method (DAKOTA's OPT++ library [14]) based on the Broyden-Fletcher-Goldfard-Shanno (BFGS) variable-metric algorithm, and the line searching approach of More and Thuente [15].

Utilizing the objective function given in Eq. (17), with $f_1 = 300\ THz$ and $f_2 = 700\ THz$, the optimization was performed using different numbers of design variables. Increasing the number of design variables allows for greater geometric flexibility. Figure 2 illustrates the optimization results with 1, 3, and 9 design variables. As seen in Fig. 2 (a), at 426 THz no reflection can be observed from the electric field distribution for the initial model, while high reflection can be observed for the optimized geometries in Figs. 2 (b)-(d) using different number of design variables.

As shown in Fig. 3, the FWHM of reflection for the all-dielectric metamaterial increases from 111 THz to 277 THz, 285 THz, and 303 THz with 1, 3, and 9 design variables, respectively. For the optimized result with 9 design variables, the FWHM of reflection ranges from 376 to 679 THz. As shown in Fig. 4, the electric field distributions at 404 THz, 505 THz and 620 THz are simulated to demonstrate the high reflection property of the optimized metamaterial over the wide frequency range.

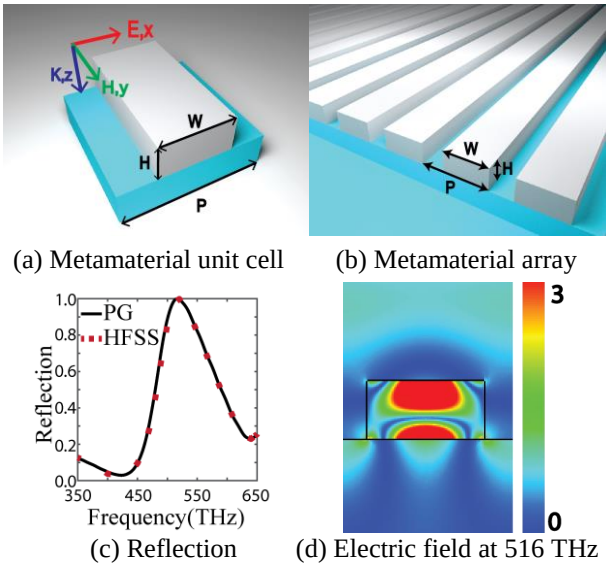

(a) Metamaterial unit cell (b) Metamaterial array

(c) Reflection (d) Electric field at 516 THz

Fig. 1. Proposed initial metamaterial model.

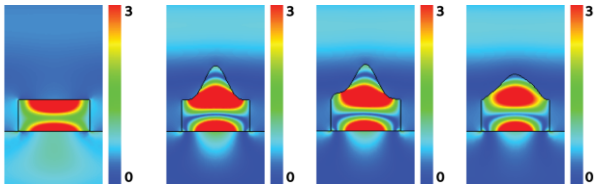

(a) Original (b) 1 dv (c) 3 dv (d) 9 dv

Fig. 2. Electric field distribution at 426 THz.

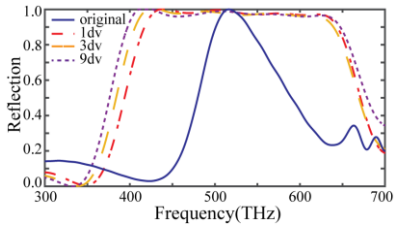

Fig. 3. Comparison of reflection over 300-700 THz.

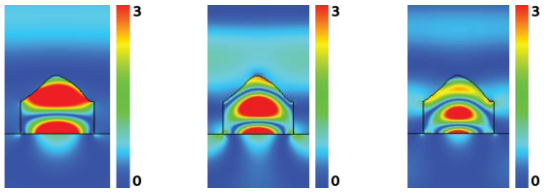

(a) 404 THz (b) 505 THz (c) 620 THz

Fig. 4. Electric field distribution of model with 9dv.

V. CONCLUSION

This paper presents an unsteady discrete adjoint approach for performing sensitivity analysis as required by gradient-based optimization algorithms. The simulations are performed by discretizing the source-free Maxwell equations using a Petrov-Galerkin finite-element method. Temporal accuracy is achieved with an implicit, second-order backward differentiation formula (BDF2). Electromagnetic shape optimization is conducted on an all-dielectric metamaterial working at optical frequencies, and considers multiple numbers of design variables. Furthermore, utilizing the current shape optimization procedure the FWHM of reflection was increased from 111 THz to 303 THz.

ACKNOWLEDGMENT

This work was supported by the THEC Center of Excellence in Applied Computational Science and Engineering. This support is greatly appreciated.

REFERENCES

[1] W. K. Anderson, L. Wang, S. Kapadia, C. Tanis, and B. Hilbert, "Petrov-Galerkin and discontinuous-Galerkin methods for time-domain and frequency-domain electromagnetic simulations," *J. Comput. Phys.*, vol. 230, pp. 8360-8385, 2011.

[2] W. K. Anderson, L. Wang, J. C. Newman III, and S. Kapadia, "Extension of the Petrov-Galerkin time-domain algorithm for dispersive media," *IEEE Microw. Wirel. Compon. Lett.*, vol. 23, no. 5, pp. 234-236, 2013.

[3] W. Lin, W. K. Anderson, J. C. Newman III, and X. Zhang, "Shape optimization of two-dimensional acoustic metamaterials and phononic crystals with a time-dependent adjoint formulation," *AIAA Paper 2016-3830*, 2016.

[4] W. Lin, J. C. Newman III, W. K. Anderson, and X. Zhang, "Broadband shape and topology optimization of acoustic metamaterials and phononic crystals," *AIAA Paper* 2016-3216, 2016.

[5] R. A. Shelby, D. R. Smith, and S. Schultz, "Experimental verification of a negative index of refraction," *Science*, vol. 292, pp. 77-79, 2001.

[6] J. Valentine, S. Zhang, T. Zentgraf, E. Ulin-Avila, D. A. Genov, G. Bartal, and X. Zhang, "Three-dimensional optical metamaterial with a negative refractive index," *Nature*, vol. 455, no. 7211, pp. 376-379, 2008.

[7] W. Li and J. Valentine, "Metamaterial perfect absorber based hot electron photodetection," *Nano Lett.*, vol. 14, no. 6, pp. 3510-3514, 2014.

[8] X. Liu, T. Tyler, T. Starr, A. F. Starr, N. M. Jokerst, and W. J. Padilla, "Taming the blackbody with infrared metamaterials as selective thermal emitters," *Phys. Rev. Lett.*, vol. 107, no. 4:045901, 2011.

[9] W. Li, Z. J. Coppens, L. V. Besteiro, W. Wang, A. O. Govorov, and J. Valentine, "Circularly polarized light detection with hot electrons in chiral plasmonic metamaterials," *Nat. Commun.*, vol. 6:8379, 2015.

[10] L. Wang and W. K. Anderson, "Adjoint-based shape optimization for electromagnetic problems using discontinuous Galerkin methods," *AIAA J.*, vol. 49, no. 6, pp. 1302-1305, 2011.

[11] P. Moitra, B. A. Slovick, W. Li, I. I. Kravchencko, D. P. Briggs, S. Krishnamurthy, and J. Valentine, "Large-scale all-dielectric metamaterial perfect reflectors," *ACS Photonics*, vol. 2, no. 2, pp. 692-698, 2015.

[12] Ansoft High Frequency Structure Simulation (HFSS), ver. 12.0, Ansoft Corporation, Pittsburgh, PA, 2009.

[13] B. M. Adams, L. E. Bauman, W. J. Bohnhoff, K. R. Dalbey, M. S. Ebeida, J. P. Eddy, M. S. Eldred, P. D. Hough, K. T. Hu, J. D. Jakeman, L. P. Swiler and D. M. Vigil, "DAKOTA: version 5.2 user's manual," *Sandia Tech. Rep.*, SAND2010-2183, 2009.

[14] J. C. Meza, R. A. Oliva, P. D. Hough, and P. J. Williams, "OPT++: An object oriented toolkit for nonlinear optimization," *ACM Trans. Math. Software*, vol. 33, no. 2, pp. 126-136, 2007.

[15] J. J. More and D. J. Thuente, "Line search algorithms with guaranteed sufficient decrease," *ACM Trans. Math. Software*, vol. 20, pp. 286-307, 1994.

A Non-Focal Rotman Lens Design to Support Cylindrically Conformal Array Antenna

Toan K. Vo Dai *, Tuan Nguyen, and Ozlem Kilic

Department of Electrical Engineering and Computer Science
The Catholic University of America, Washington, DC 20064, USA
*30vodai@cua.edu

Abstract ─ Rotman lenses offer broad bandwidth, and render to planar structures making them ideal for a variety of applications. However, a limitation of the Rotman lens is that it is based on the assumption of supporting linear arrays. In this paper, we develop a new design technique to enable the lens to feed a conformal array antenna.

Index Terms ─ Beam Forming Networks (BFNs), conformal array antennas, Particle Swarm Optimization (PSO), Rotman lens.

I. INTRODUCTION

Rotman lens, which was invented by Rotman and Turner in 1962, is an analog beam former that creates a specific phase taper at its output ports to feed an array antenna. Based on the input parameters (such as the scanning angle (φ), the focal angle (α), number of input and output ports; the lens equations can be solved to determine its receive contour, delay lines (w_i) and the focal arc to generate a desired phase taper [1]. In the past few decades, numerous Rotman lens designs have been developed [2-5]. However, a limitation of these designs is the assumption of a uniform linear array at the output ports. This prohibits their applications to conformal array antennas.

The ability to feed conformal array antennas with a Rotman lens would be of interest as these systems can be applied to a variety of applications such as antennas residing on the surface of an airplane's wing, the body of a missile or a high-speed train, which are used for communications or navigation purposes. In this paper, we develop a new design inspired by Rotman lens to feed a cylindrically conformal array. We solve for the lens equations to satisfy the constraints of the design by employing the Particle Swarm Optimization (PSO) [4]. Our approach applies to other conformal geometries as well. For the purposes of this paper, we will use our method to design a lens with 3 input ports feeding an 8-element conformal array operating at a center frequency of 10 GHz.

The remainder of the paper is organized as follows. Section II introduces the overview of our system design. Section III gives a brief overview of the PSO algorithm. Section IV discusses the optimization of phase values for the conformal array, and Section V reviews the proposed design procedure of the non-focal lens. The performance of the optimization process is discussed in Section VI. Simulation results are presented in Section VII, followed by the conclusions in Section VIII.

II. OVERVIEW OF THE SYSTEM DESIGN

In this paper, we demonstrate the design of a Rotman lens inspired, non-focal microwave lens to support an array conforming to a cylindrical surface as shown in Fig. 1.

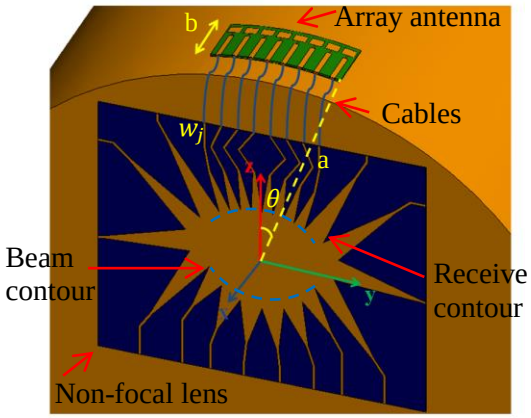

Fig. 1. Overall system design.

Two tasks are considered in order to design the lens. The first task is to optimize the required phase information to scan the conformal array in the desired directions. The second task is to use the phase information obtained in the first task as an objective function to design the non-focal lens that generates the desired phase values identified in the first task. Both tasks require an optimization method for which we choose PSO for its

Submitted On: July 12, 2016
Accepted On: August 30, 2016

ease of use and reliable performance. The optimization in the first task is straightforward while the second task can be challenging as it involves numerous variables to be optimized under a set of constraints.

III. OVERVIEW OF PSO

Particle Swarm Optimization (PSO) is a random search algorithm, which simulates the behavior of bees in their search for the best location in the field [6]. As with all random search algorithms, the objective is to minimize a cost function defined for the specific problem. In the optimization process, the bees sample the optimization space and decide where to go next as they search for the best location based on the collective intelligence of the swarm and their personal experiences. The velocity that determines the next position of an agent is based on these two factors and the user defined constants w, c_1, c_2, which correspond to the weights of velocity along the original direction of the bee and towards the personal and global best values, respectively. The user also specifies the total number of agents, maximum number of iterations for termination and the boundary conditions for the search space.

IV. OPTIMIZATION OF PHASE EXCITATION FOR CONFORMAL ARRAY

Our design of the cylindrically conforming array antenna is based on the parameters shown in Fig. 1, where a is the radius of the cylinder, b represents the width of the array, and θ is the angle measured with respect to the z-axis in radians, and determines the total length l of the array by the relation: $l = 2a\theta$. The phase distribution for each element of the array to acquire the desired scan direction depends on the curvature characteristics of the surface it resides on.

Our paper investigates two different array geometries as depicted in Table 1. Both arrays will be designed at a center frequency of 10 GHz; the center-to-center spacing between the radiating elements is $\lambda_0/2$ (where λ_0 is the wavelength at 10 GHz).

Table 1: Design parameters of array for two cases

Parameters	Case 1	Case 2
θ (°)	16	32
a (cm)	30	15
b (cm)	5	5
l (cm)	16.8	16.8

In this paper, we first employ PSO to optimize the phase distribution for the 8-element conformal array for a desired scanning angle. The desired scan positions are [-30°, 0, 30°], where the angle is calculated with respect to the z-axis. This results in 8 variables in the interval of [0, 2π] to be optimized for each scan position. We employ 100 agents, and terminate the search after 500 iterations. The user defined parameters $c_1 = c_2$ and w are chosen to be 2 and 0.9, respectively. We minimize the cost function as given in (1) to achieve the desired solution:

$$F(\vec{\alpha}) = w(|SLL|_{dB} - |SLL_{max}|_{dB}) - Gain(\theta, \phi, \vec{\alpha}), \quad (1)$$

where *Gain* is the power gain in the (θ, ϕ) direction, $\vec{\alpha}$ is a 24 element vector corresponding to the phase distribution for each input port, SLL_{dB} refers to sidelobe levels achieved from the PSO algorithm and SLL_{maxdB} is the maximum level allowed. The PSO stops the search when F ≤ -15 dB (when Gain ≥ 15 dB and SLL_{dB} achieved is approximately equal SLL_{maxdB} required) or the maximum number of iterations is reached. The radiation patterns of arrays for both cases are shown in Figs. 2 (a) and 2 (b), respectively. The maximum gain we obtain is 15 dB for each scanning angle while the SLL is about 10 dB down from the peak.

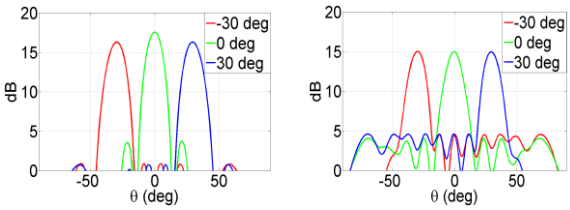

(a) (b)

Fig. 2. Radiation pattern of conformal array in: (a) case 1 and (b) case 2.

V. OPTIMIZATION OF THE NON-FOCAL LENS

Figure 3 shows a general concept of the optimized lens. Due to the curvature dependence of the phase values feeding the conformal array, it is not possible to directly apply the Rotman lens formulation in [1] to solve for the receiving contour, delay lines and beam contour since the Rotman lens formulation assumes a linear array at its output. We modify the general equations in finding the path length from an input port on the beam contour to an output port on the receiving contour. By optimizing the locations of input and output ports as well as the delay lines, we obtain the expected phase value at the input of conformal array as described in (2):

$$\phi_{i,j} = k_r \sqrt{(x_j - x_{fi})^2 + (y_j - y_{fi})^2} + k_{eff}.w_j, \quad (2)$$

where (x_{fi}, y_{fi}) is the coordinate of the input port, (x_j, y_j) is the coordinate of the output port, w_j is the length of the delay line corresponding to each output port, $k_r = \frac{2\pi}{\lambda}\sqrt{\varepsilon_r}$ and $k_{eff} = \frac{2\pi}{\lambda}\sqrt{\varepsilon_{eff}}$ where λ is the free space wavelength at the center frequency and ε_{eff} is the effective dielectric constant of the microstrip line feeding the array.

In our formulation, we assume that the receiving contour lies on an ellipse. This constraint ensures a

smooth curvature at the output. There are a variety of options in choosing the shape of the receiving contour. We choose an elliptical arc because it resembles the shape in a conventional Rotman lens. As shown in Fig. 3, we have 24 variables to optimize, which include the coordinates of input ports ($x_{f1} \dots x_{f3}$, $y_{f1} \dots y_{f3}$), y-coordinates of output ports ($y_1 \dots y_8$), radii of elliptical receiving contour (l_1, l_2) and corresponding delay line lengths ($w_1 \dots w_8$). For cases with higher number of input or output ports, the number of optimization variables increase, which would inevitably slow down the convergence of the PSO to good solutions.

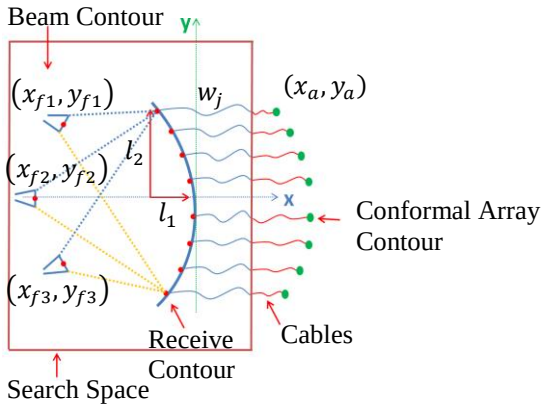

Fig. 3. Concept of non-focal lens design.

The fundamental challenges of this problem are how to design a lens so that it not only supports a conformal array, but is also practical for fabrication. Thus, we must implement a suitable cost function in PSO to guarantee a smooth curvature, and to position all output ports well for maximum power reception. Below are the constraints we choose for the PSO algorithm to design an appropriate lens:

i. Ports are randomly distributed on the receiving contour with spacing requirement $\boldsymbol{\lambda_r/2 \le S_i \le 3\lambda_r}$ where $\boldsymbol{\lambda_r = \lambda/\sqrt{\varepsilon_r}}$ is the effective wavelength inside the substrate, and $\boldsymbol{S_j}$ is the arc length between two adjacent output ports $\boldsymbol{(x_j, y_j)}$ and $\boldsymbol{(x_{j+1}, y_{j+1})}$. The minimum spacing between two adjacent ports is $\boldsymbol{\lambda_r/2}$ to make sure that it is posible for the lens to be fabricated while the maximum spacing is $\boldsymbol{3\lambda_r}$ constrains the overall dimensions of the lens.

ii. Beam ports are positioned randomly with a constraint on the minimum distance between each pair, such that $\boldsymbol{d_i = \sqrt{(x_{fi} - x_{fi+1})^2 + (y_{fi} - y_{fi+1})^2} \ge \frac{\lambda_r}{4}}$. Unlike the conventional lens, our approach has no limitations for the beam ports to lie on a circular or elliptical arc.

iii. An important constraint is to make sure beam ports do not block each other. We define an illuminating region from a beam port to the output ports (the regions are separated by the dashed blue and solid yellow lines as shown in Fig. 3). If the other input ports happen to lie in this region, the PSO algorithm will not accept these cases as solutions.

VI. PERFORMANCE OF PSO

After all the constraints are satisfied, the phases at the output ports are calculated and compared with the set of desired phase values to assess the cost function for this optimization problem. We use 600 agents and a maximum of 10000 iterations, where the user defined variables are chosen as $c_1 = c_2 = 2$ and $w = 0.9$. The optimization aims to minimize the cost function (3):

$$F = \sqrt{\sum_{i=1}^{N_{input}} \sum_{j=1}^{N_{output}} \left(\phi_{i,j} - \phi_{i,jref}\right)^2}, \qquad (3)$$

where $\phi_{i,j}$ is calculated in (2) and $\phi_{i,jref}$ is the desired phase values. To limit the overall dimensions of the lens, we set the search space for input ports, output ports and length of a delay line in appropriate intervals. For example, for a 3-input, 8-output Rotman lens, we would want $x_{fi} \in [-10\lambda_r, 0]$, $y_{fi}, y_j \in [-10\lambda_r, 10\lambda_r]$, $a, b \in [4\lambda_r, 10\lambda_r], w_j \in [\lambda_r, 10\lambda_r]$. Figure 4 shows the convergence rate of the optimized lens in case 1 and 2 over 10000 iterations.

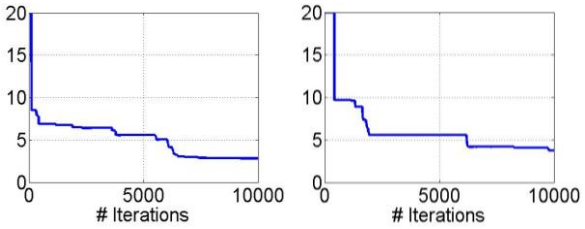

Fig. 4. Performance of PSO for optimized lens in case 1 and case 2.

VII. RESULTS FOR NON-FOCAL LENS

To verify the robustness of our lens design, we design a 3-input, 8-output used to feed a slightly bent conformal array with parameters specified in case 1 and case 2, Table 1. The substrate we are using is Duroid 5880 with $\varepsilon_r = 2.2$. Figures 5, 6 show the simulation model of the lens using commercial software package FEKO and its performance over a bandwidth from 9 GHz to 11.5 GHz. Figures 7, 8 show the radiation pattern of the array fed by the output of the lens at 10 GHz.

The overall dimensions of the non-focal lens design in each case are greater compared with the conventional Rotman lens working at 10 GHz and using the same substrate.

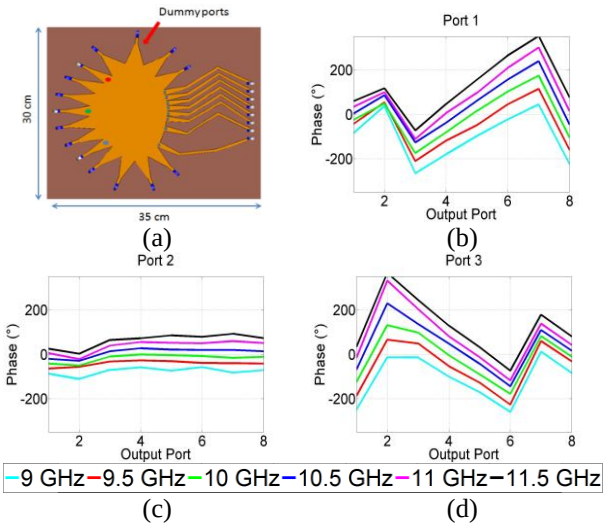

Fig. 5. 3-input, 8-output lens to feed conformal array in case 1: (a) CAD model, phase performance, (b) Port 1, (c) Port 2, and (d) Port 3.

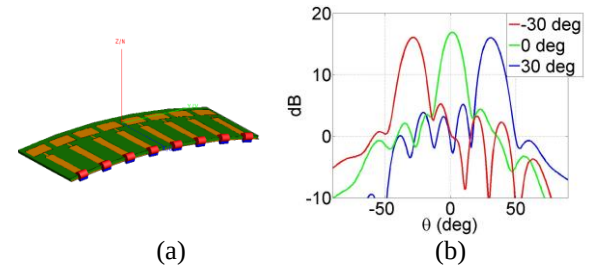

Fig. 6. (a) Bent array in case 1, and (b) radiation pattern of the array at -30°, 0°, 30°.

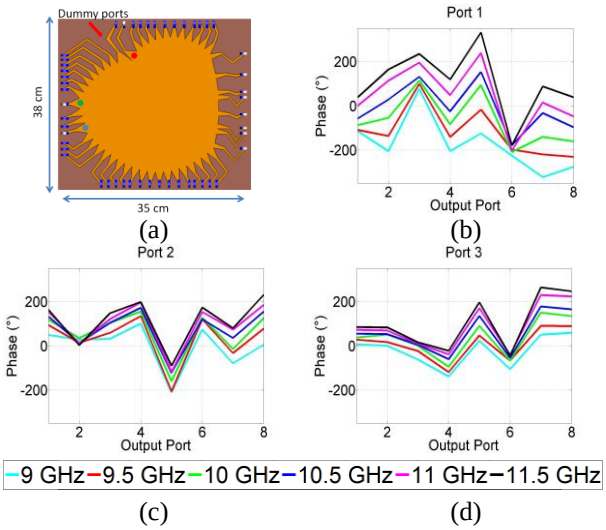

Fig. 7. 3-input, 8-output lens to feed conformal array in case 2: (a) CAD model, phase performance, (b) Port 1, (c) Port 2, and (d) Port 3.

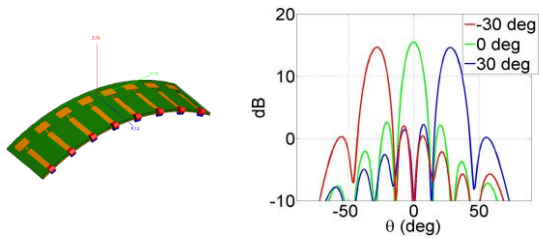

Fig. 8. (a) Bent array in case 2, and (b) radiation pattern of the array at -30°, 0°, 30°.

VIII. CONCLUSIONS

In this work, we investigated a new design technique to extend the design equations of Rotman lens to feed conformal array antennas. The applicability was shown using a cylindrical curvature, but the method applies to other curvatures as well. The results show that with similar total dimensions compared with conventional Rotman lens working at the same frequency and substrate, this lens design is able to support a cylindrical array. The proposed design works with any array antenna on different singly curved surfaces. While the concept has been shown for a 3-input port lens, the optimization can be run for higher number of input and output ports. However, for such cases, the number of optimization variables increase, which would inevitably slow down the convergence of the PSO algorithm to good solutions.

REFERENCES

[1] W. Rotman and R. Turner, "Wide-angle microwave lens for line source applications," *IEEE Transactions on Antennas and Propagation*, vol. 11, pp. 623-632, 1963.

[2] M. S. Smith, "Design considerations for Ruze and Rotman lenses," *Radio and Electronic Engineer*, vol. 52, no. 4, pp. 181-187, 1982.

[3] R. C. Hansen, "Design trades for Rotman lenses," *IEEE Transactions on Antennas and Propagation*, vol. 39, no. 4, pp. 464-472, 1991.

[4] O. Kilic and S. Weiss "Rotman lens designs for military applications," *Radio Science Bulletin*, no. 333, pp. 10-24, 2010.

[5] J. Dong and A. I. Zaghloul, "Non-focal 2D Rotman lens design," *IEEE Transactions on Antennas and Propagation*, 2008.

[6] J. Kennedy and R. C. Eberhart, "Particle swarm optimization," in *Proc. IEEE Conf. Neural Networks IV*, Piscataway, NJ, 1995.

Efficient MCF Evaluation in a Turbulent Atmosphere over Large Structure Constant Interval

Naser A. Abu-Zaid

Department of Electrical and Communications Engineering
An-Najah National University, Nablus, P.O. Box 7, West Bank
naser_res@yahoo.com, naserzaid@najah.edu

Abstract ─ A fast and accurate method is derived and simulated to compute the mutual coherence function (MCF) of an electromagnetic beam wave propagating through atmospheric turbulence over a large interval of structure constant. This method is based on expanding the integral equation solution for one value of structure constant into its Pade' approximation to cover large fluctuation interval. The expansion is compared with numerical results, and a very good agreement was obtained. Such computations are important in practical fields as remote sensing, imaging systems, and optical communications.

Index Terms ─ Atmospheric scattering, atmospheric turbulence, coherence, mutual coherence function, Pade' approximation.

I. INTRODUCTION

Electromagnetic wave scattering problem by a turbulent atmosphere was solved several decades ago [1], and does not represent a challenging problem anymore. Solutions were over and done with the Rytov method or by perturbation theory for several moments such as the second order statistical moment known as mutual coherence function (MCF) [1, 2]. MCF within Rytov approximations were compared to that which resulted from the parabolic equation for the case of weak and strong fluctuations, including cases of plane, spherical and beam waves [3]. In recent years, the advent of advanced processors and modern applications in astronomy, remote sensing, free space optical communications, and imaging [4] renewed the interest in atmospheric scattering of beam electromagnetic waves. Consequently, finite element methods [5] and finite difference methods [6] were applied extensively to solve the scattering problem [7].

In all mentioned methods, field solutions were obtained for a single value of structure constant or at a single or double excitation frequencies, and none were obtained over an interval of structure constant. Several authors succeeded in obtaining the solution over wide range of frequency [8], and over a range of complex permittivity [9]. Nevertheless, those methods dealt with deterministic media. In this work, solution for MCF is found over a continuous interval of structure constant in a turbulent atmosphere. The solution method is based on computing the MCF integral at a single value of structure constant, expanding integral solution into its truncated power series, finding power series coefficients from which Pade' approximants [10] are calculated, then approximations are established.

Generally, solving Maxwell's equations or the wave equations for non-symmetric geometries or obstacles usually requires resorting to numerical techniques. Domain discretization in such techniques, in either finite difference methods or finite element methods, is a necessity. Such procedures consume computer time and memory, especially for large scale problems, which put limits on the electrical size of problems under study, specifically when the solution is required for several values of some parameter of interest. Pade' approximation offers a method of reducing computer CPU time and memory, while maintaining the high accuracy of the solution.

II. FORMULATION

Consider a beam electromagnetic wave propagating along the z direction in a randomly turbulent atmosphere. The wave length is assumed to be much smaller than eddies forming fluctuating permittivity field. Such wave satisfies the stochastic Helmholtz equation [1-3]:

$$\nabla_t^2 U(\boldsymbol{\rho}) + 2jk\frac{\partial U(\boldsymbol{\rho})}{\partial z} + k^2\tilde{\varepsilon}(\boldsymbol{\rho})U(\boldsymbol{\rho}) = 0, \qquad (1)$$

where $\tilde{\varepsilon}$ is the stochastic permittivity field, ∇_t^2 is the transverse scalar Laplacian, $\boldsymbol{\rho}$ is the transverse radial vector, j is the imaginary unit, $U(\boldsymbol{\rho})$ is the transverse electric field component, $k = 2\pi/\lambda$ is the free space wave number, and λ is the free space wave length. The important parameter of interest characterizing such waves, is the mutual coherence function MCF, defined [1, 2]:

$$\Gamma_2(\boldsymbol{\rho}_1, \boldsymbol{\rho}_2, z) = \langle U(\boldsymbol{\rho}_1, z)U^*(\boldsymbol{\rho}_2, z)\rangle, \qquad (2)$$

where $\langle\cdot\rangle$ represent ensemble average, $\boldsymbol{\rho}_1 = x_1\hat{x} + y_1\hat{y}$, $\boldsymbol{\rho}_2 = x_2\hat{x} + y_2\hat{y}$, and U^* indicates conjugation. Assuming

Submitted On: July 30, 2016
Accepted On: September 9, 2016

a beam with Gaussian amplitude distribution at the transmitting aperture $z = 0$, with a waist radius w_o and a phase front with radius of curvature R_o, an expression for MCF within the second order Rytov approximation was derived and evaluated for a beam wave propagating through a turbulent atmosphere [1-3]:

$$\Gamma_2(\boldsymbol{\rho}_c, \boldsymbol{\rho}_d, z) = \frac{w_o^2}{w^2} exp(g_1) exp(g_2),$$

$$g_1 = -\frac{k}{2}\left(\frac{w_o^2}{w^2}\right)(g_3 - j2g_4),$$

$$g_2 = -4.352 k C_n^2 \int_0^{L_z} \left(\gamma_I(z)\frac{L_z - z}{k}\right)^{5/6} {}_1\mathrm{F}_1\left(-\frac{5}{6}, 1; g_5\right) dz,$$

$$g_5 = -\frac{k|\gamma_R \boldsymbol{\rho}_d - j2\gamma_I \boldsymbol{\rho}_c|^2}{4\gamma_I(z)(L_z - z)},$$

$$g_3 = 2\alpha_1\left(\rho_c^2 + \frac{\rho_d^2}{4}\right),$$

$$g_4 = [\alpha_2 - (\alpha_1^2 + \alpha_2^2)L_z](\boldsymbol{\rho}_c \cdot \boldsymbol{\rho_d}),$$

$$w^2 = w_o^2\left[(1 - \alpha_2 L_z)^2 + \alpha_1^2 {L_z}^2\right],$$

$$\boldsymbol{\rho}_c = \frac{\boldsymbol{\rho}_1 + \boldsymbol{\rho}_2}{2},$$

$$\boldsymbol{\rho}_d = \boldsymbol{\rho}_2 - \boldsymbol{\rho}_1,$$

$$\alpha = \alpha_1 + j\alpha_2 = \frac{2}{k w_o^2} + j\frac{1}{R_o},$$

$$\gamma(z, L_z) = \frac{1 + j\alpha z}{1 + j\alpha L_z} = \gamma_R - j\gamma_I, \qquad (3)$$

where ${}_1F_1$ is the confluent hypergeometric fuction, C_n^2 is the refractive index structure constant, L_z is the distance from the output aperture. Expanding the unknown MCF in Eq. (3) into its power series about an arbitrary structure constant C_{no}^2, as:

$$\Gamma_2 = \sum_{i=0}^{\infty} a_i (C_n^2 - C_{no}^2)^i, \qquad (4)$$

where

$$a_i = \frac{1}{i!}\frac{\partial \Gamma_2}{\partial C_n^2}\bigg|_{C_n^2 = C_{no}^2}$$

$$= \frac{1}{i!}\frac{w_o^2}{w^2}\left(\frac{1}{C_n^2} g_2\right)^i exp(g_1) exp(g_2)\bigg|_{C_n^2 = C_{no}^2}. \qquad (5)$$

$[L/M]$ Pade' approximants are obtained by truncating the power series at N, then matching to a rational:

$$\sum_{i=0}^{N} a_i (C_n^2 - C_{no}^2)^i \approx \frac{\sum_{l=0}^{L} p_l (C_n^2 - C_{no}^2)^l}{1 + \sum_{m=1}^{M} q_m (C_n^2 - C_{no}^2)^m}. \qquad (6)$$

$N + 1$ equations reached from expansion of Eq. (6). The $q's$ are attained from the last M of these equations:

$$\begin{bmatrix} q_1 \\ q_2 \\ \vdots \\ q_M \end{bmatrix} = -\begin{bmatrix} a_L & a_{L-1} & \dots & a_{L-M+1} \\ a_{L+1} & a_L & \dots & a_{L-M} \\ \vdots & \vdots & & \vdots \\ a_{L+M-1} & a_{L+M-2} & \dots & a_L \end{bmatrix}^{-1} \begin{bmatrix} a_{L+1} \\ a_{L+2} \\ \vdots \\ a_{L+M} \end{bmatrix}, \qquad (7)$$

whereas the $p's$ are found from the rest of equations:

$$\begin{bmatrix} a_o & 0 & \dots & 0 \\ a_1 & a_o & \dots & 0 \\ \vdots & \vdots & & \vdots \\ a_L & a_{L-1} & \dots & a_o \end{bmatrix} \begin{bmatrix} 1 \\ q_1 \\ \vdots \\ q_L \end{bmatrix} = \begin{bmatrix} p_o \\ p_1 \\ \vdots \\ p_L \end{bmatrix}. \qquad (8)$$

III. NUMERICAL APPLICATIONS AND VALIDATION

With the derivation of asymptotic expansion coefficients accomplished, an investigation must now be made with regard to their applicability and validity. To demonstrate the efficiency of the technique, three simulations will be carried out on a 1.6 GHz personal computer. In all simulations, 41 structure constant values and 9 transverse space points are implemented for direct numerical solution. As a first check, power series expansion around $C_{n0}^2 = 10^{-16}$ with $[2/5]$ Pade' approximants used, and both expansions compared with direct numerical solution as shown in Fig. 1. The propagation parameters given by $w_0 = 0.05\,m$, $L_z = 2.5\,km$, $\lambda = 630\,nm$. It requires 145.9531s to obtain the solution with direct solution, though, it only takes 4.3281s for single point expansion. It may be inferred that the power series approximates well for small values of C_n^2, but drops sharply for larger values, while Pade' expansions shows very good approximation even deep in lager C_n^2 values region.

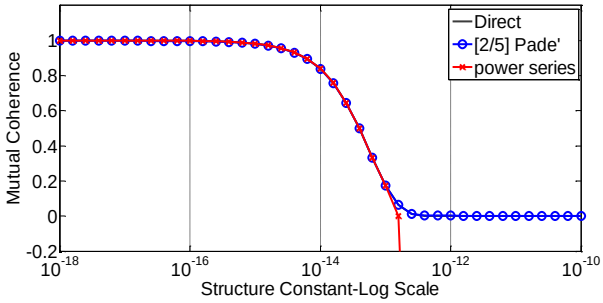

Fig. 1. Normalized mutual coherence function $\Gamma_2(0,0,L_z)$ versus C_n^2.

In Fig. 2, simulation parameters are $C_{n0}^2 = 10^{-16}$ $w_0 = 0.005\,m$, $L_z = 2.5\,km$, $\lambda = 630\,nm$. To study the effect of numerator and denominator degrees on quality of Pade' expansions, three different values are taken, namely, $[L/M] = [3/3]$, $[L/M] = [2/4]$ and $[L/M] = [4/2]$. Simulations show that when the denominator degree is larger than numerator degree, Pade' expansions approximated the solution very well. In the contrary, other orders did not for larger values of C_n^2, the approximation skyrockets when numerator degree is larger, and drops steeply when numerator and denominator degrees are equal. The difference in time between the three cases is a fraction of a second and can be neglected. However, it should be noted that as the number of power series coefficients is increased to larger integers, their values become very prohibitive and Pade' matrix becomes close to singular. This is expected since their values increase as powers of wave number.

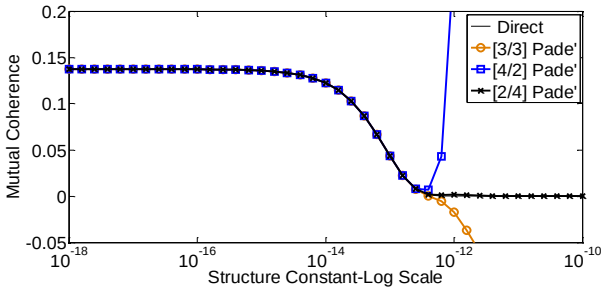

Fig. 2. Normalized mutual coherence function $\Gamma_2(\rho_c = 0.1,0,L_z)/\Gamma_2(0,0,L_z)$ versus structure constant C_n^2 for different Pade' orders.

Turning into another case, and shifting the expansion point toward larger fluctuations, namely, $C_{n0}^2 = 10^{-14}$, as shown in Fig. 3. An obvious observation is that power series does not approximate in larger fluctuations region, and has an almost constant error in smaller fluctuations region, which is expected, since the solution has almost constant slopes for smaller fluctuations. Amazingly enough, Pade' expansions agrees very well with direct solution for both small and large fluctuations. Simulation parameters given by $w_0 = 0.05\ m$, $L_z = 2.5\ km$, $\lambda = 630\ nm$, $[L/M] = [2/5]$.

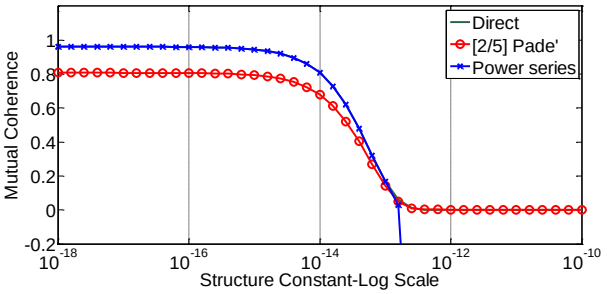

Fig. 3. Mutual coherence function $\Gamma_2(0,0,L_z)$ versus structure constant C_n^2 for a different expansion point $C_{n0}^2 = 10^{-14}$.

IV. CONCLUSION

Numerical methods offer a strong technique to compute the mutual coherence function of electromagnetic beam waves scattered by atmosphere. The efficiency is extremely increased when combined with Pade' approximation. It is shown that direct solution takes about 32 times the required time for Pade' expansion in presented simulations. In this research, it is also shown that a rational expansion with denominator degree larger than numerator gives much more accurate solution. Finally, rational asymptotes work very fine for small fluctuations region as well as for larger fluctuations.

REFERENCES

[1] V. Tatarski, *Wave Propagation in a Turbulent Medium*. McGraw-Hill Translation, 1961.

[2] A. Ishimaru, *Wave Propagation and Scattering in Random Media*. Academic Press, 1978.

[3] R. M. Manning, "Beam wave propagation within the second Rytov perturbation approximation," *Radiophysics and Quantum Electronics*, pp. 287-295, 1996.

[4] X. Zhu and J. Khan, "Performance bounds for coded free-space optical communications through atmospheric turbulence channels," *IEEE Transactions on Communications*, pp. 1233-1239, 2003.

[5] J. Jin, *The Finite Element Method in Electromagnetics*. Wiley, 2002.

[6] A. Taflove and S. Hagness, *Computational Electrodynamics: The Finite-Difference Time-Domain Method*. Artech House, 2005.

[7] T. Wang and D. Zhao, "Scattering theory of stochastic electromagnetic light waves," *Optics Letters*, vol. 35, 2010.

[8] M. Kuzuoglu and R. Mittra, "Finite element solution of electromagnetic problems over a wide frequency range via the Pade' approximation," *Comput. Methods Appl. Mech. Eng.*, pp. 263-277, 1999.

[9] N. Abu-Zaid and H. Tosun, "Finite element analysis of two dimensional electromagnetic scattering via Pade' approximation for complex permittivity," *Radio Science*, vol. 37, no. 1, 2002.

[10] G. Baker and B. Graves-Morris, *Pade' Approximants*. Cambridge Univ. Press, 1996.

Multi-Frequency T-Slot Loaded Elliptical Patch Antenna for Wireless Applications

S. Murugan, B. Rohini, P. Muthumari, and M. Padma Priya

Department of ECE, K.L.N. College of Engineering, Pottapalayam-630612, Sivagangai District, India
murugans1976@gmail.com, rohinibala17@gmail.com, muthumariengg@gmail.com,
padma.nmanickam@gmail.com

Abstract **–** In this paper, a multi frequency microstrip antenna (MSA) for wireless applications is designed. The proposed MSA comprised of elliptical patch antenna with T-slot. This antenna is fed by coaxial probe. The design parameters are major and minor axis of elliptical patch, length and width of T-slot and feeding point of probe. The proposed antenna can provide optimized multi frequency by varying the above design parameters. FR-4 substrate with dielectric constant 4.4 is chosen. The multi frequencies are 1.57 GHz, 1.96 GHz and 3.4 GHz, which covers the applications such as GPS and 4G LTE. The simulation of the antenna is performed using the ANSOFT HFSS and it is analyzed for S_{11} (dB) and radiation pattern. The prototype antenna is fabricated for optimized dimensions and tested using vector network analyzer. Simulation and experimental results are compared with each other.

Index Terms **–** Coaxial feed, elliptical patch antenna, multi-frequency, T-slot.

I. INTRODUCTION

The microstrip antenna (MSA) is one of the most preferred antenna structures for wireless applications and handheld devices. They are small in size, light weight and low volume. Generally, the multi-frequency MSA are divided into two categories: i) multi-resonator antennas and reactively loaded antenna. In the first category, the multi-frequency operation is achieved by means of multiple radiating elements, each supporting strong currents and radiation at its resonance. It includes the multilayer stacked-patch antennas using circular, annular, rectangular and triangular patches [1], [2]. A multi-resonator antenna in coplanar structures can also be fabricated by using aperture-coupled parallel microstrip dipoles [3]. As these antenna structures usually involve multiple substrate layers, they are of high cost. Large size is another drawback of the multi-resonator antenna, which makes it difficult for the antenna to be installed in hand-held terminals. The second category is reactively load MSA, to obtain multi frequency operation of the antenna such as multi-slotted patch, rectangular patch with two T-slots, truncated circular patch with double U-slot, square spiral patch antenna and pi-shaped slot on rectangular patch [4-9]. These structures involve complex calculation, design, higher frequency ratio and lower bandwidth as compared to proposed antenna. Therefore, the proposed antenna consists of a simple T-slot which is loaded on the elliptical patch antenna and it is fed by coaxial probe. The dimensions of the proposed antenna are optimized using HFSS in such a way that it provides multi-frequency. The paper is organized as, proposed antenna design is discussed in Section 2, followed by simulation and experimental results in Section 3, and Section 4 concludes the paper.

II. ANTENNA DESIGN

The proposed antenna is shown in Fig. 1 (top view) and Fig. 2 (side view). The elliptical patch of semi major axis ‘a’ and semi minor axis ‘b’ is printed on the FR-4 substrate (ε_r=4.4). A T-slot of length ‘l’ and width ‘w’ is slotted in the elliptical patch.

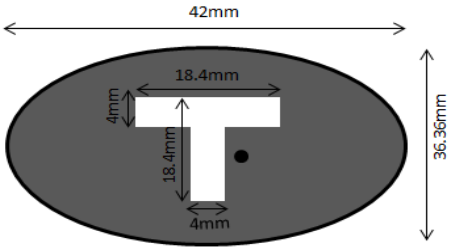

Fig. 1. Top view of proposed antenna.

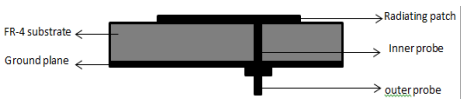

Fig. 2. Side view of proposed antenna.

The resonant frequency of elliptical patch is given as [10]:

$$fr = \frac{c\sqrt{q}}{\pi a e \sqrt{\varepsilon_r}}, \quad (1)$$

Submitted On: August 13, 2016
Accepted On: September 11, 2016

where c is velocity of light, ($3*10^8$ m/s), e is eccentricity of elliptical patch as:

$$e = \sqrt{1 - (b|a)^2}, \quad (2)$$

where 'a' is the semi major axis of the elliptical patch, 'b' is semi minor axis of the elliptical patch, $\boldsymbol{\varepsilon}_r$ is dielectric constant of the substrate, q is the approximated Mathieu function of the given mode and eccentricity is calculated from [11]. The order of few modes of elliptical patch antenna is TM_{11} and TM_{21} and is based on the q value function. In this paper, TM_{11} mode is chosen. Then the q value for TM_{11} mode is given.

For the e values between 0 and 0.4:

$$q_{11} = 0.847e^2 - 0.0013e^3 + 0.0379e^4, \quad (3)$$

For the e value between 0.4 and 1.0:

$$q_{11} = -0.0064e + 0.8838e^2 - 0.0696e^3 + 0.082e^4, \quad (4)$$

Here, the eccentricity of 0.5 is chosen and the canter frequency is taken as 2 GHz. By substituting the canter frequency and eccentricity values in the above equations, the dimensions of the elliptical patch can be calculated. The T-slot length and width can be determined by parametric study.

For TM_{11} mode, the theoretical value of resonant frequency for elliptical patch of semi major axis 21 mm is found to be 2 GHz. This is the theoretical resonant frequency value for elliptical patch without T-slot. The multi frequency resonance can be obtained by properly designing the length and width of the T-slot and also the feed point of the probe. This plays a major role in optimizing the frequency.

III. SIMULATION AND EXPERIMENTAL RESULTS

The simulation of the above designed antenna was performed using ANSOFT HFSS software. The FR-4 substrate size of 10 0mm*100 mm*1.6 mm is chosen as a dielectric material. Coaxial probe is used for exciting the patch. Return loss (dB) is defined as that the difference in dB between power sent towards antenna under test (AUT) and power reflected [12]. The requirement for reflection co-efficient of wireless devices specifies 10 dB return loss bandwidth.

The parametric study of the antenna is performed using Ansoft HFSS. Table 2 shows the S_{11} (dB) values for different lengths of T slot, keeping the width constant. As the length of the T-slot is increased, the resonant frequency is decreased. The length and width of the T-slot is chosen as 17.8 mm and 4 mm to obtain the optimized desired multi-frequency. A prototype is fabricated for the dimensions given in Table 1. The photograph of the antenna is shown in Fig. 3. The fabricated antenna is tested using vector network analyzer. Figure 4 shows the comparison of both simulated and measured S_{11} (dB) vs. frequency (GHz).

Table 3 shows the comparison of simulated and measured output.

Table 1: Design specifications

Design Parameters	Values
Semi major axis 'a'	21 mm
Semi minor axis 'b'	18.18 mm
Eccentricity 'e'	0.5
Substrate thickness h	1.6 mm
Dielectric constant '$\boldsymbol{\varepsilon}_r$'	4.4
Length of the T-slot 'l'	18.4 mm
Width of the T-slot 'w'	4 mm
Feed point	(6,3)

Table 2: Parametric study (w = 4 mm)

Length (mm)	Resonant Frequencies (GHz)	Corresponding S_{11} (dB)
17.8	1.57	-31.06
	1.96	-19.83
	3.43	-21.76
17	1.58	-18.73
	1.94	-24.6
	3.25	-15.73
16.5	1.63	-16.61
	1.99	-21.06
	3,41	-15.34
16	1.67	-14.26
	1.99	-20.79
	3.4	-12.28

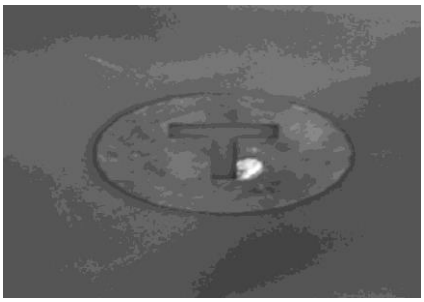

Fig. 3. Photograph of fabricated antenna.

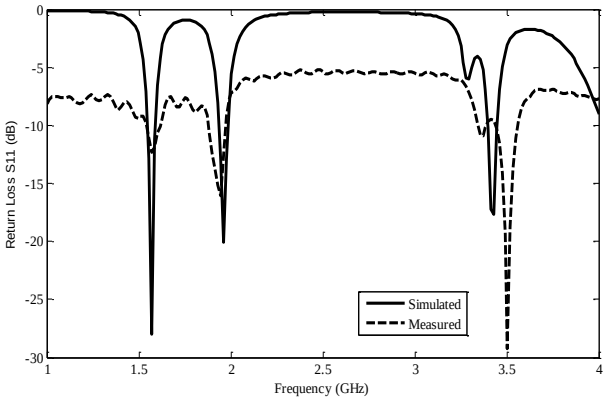

Fig. 4. S_{11} (dB) vs. frequency (GHz).

Table 3: Simulated and measured S_{11} (dB)

Parameters	Simulation Output	Measured Output
Frequency (GHz)	1.57 1.96 3.4	1.58, 1.946 3.5
S_{11} (dB)	-31.06, -19.83 and -21.76 respectively	-11.26, -16.36 and -19.09 respectively

Figure 5 shows the radiation pattern at 1.57 GHz. It is simulated using HFSS for φ=0° E plane (XZ plane) and φ=90° (YZ plane). The coordinate system is XYZ and the antenna is placed in XY plane. It has very low gain of -4.53 dB and HPBW of 84 degrees. Figure 6 shows the radiation pattern at 1.96 GHz has a very low gain of -0.3357 dB and HPBW of 84 degrees. Figure 7 shows radiation pattern at 3.43 GHz, which has butterfly pattern. FR4 is lossy substrate. The loss tangent of the substrate is high, which affects the performance of the antenna. It may be the reason for low gain. Moreover, size of the patch is very small. The gain of the antenna is directly proportional to cross sectional area of the patch. The T shaped slot is etched from this patch, which also reduces the area of the patch; hence, further reduces the gain. In [13], a truncated elliptical patch is discussed, which also has a low value of gain.

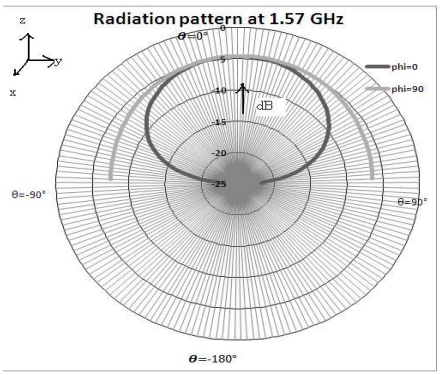

Fig. 5. Radiation pattern at 1.57 GHz.

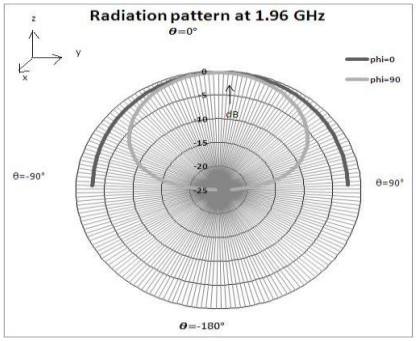

Fig. 6. Radiation pattern at 1.96 GHz.

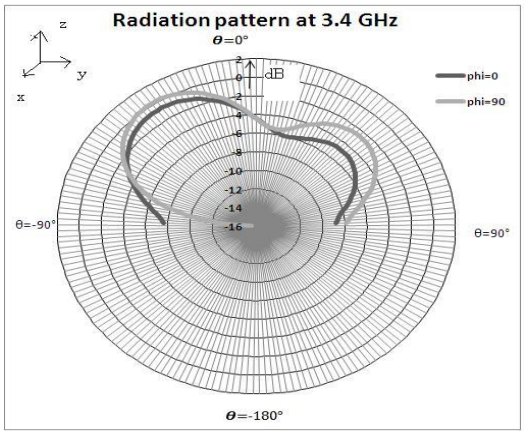

Fig. 7. Radiation pattern at 3.4 GHz.

The proposed antenna may be compared with some of antennas given in references. It is described below. In [4], multi-slotted antenna of size 39.6 mm*47.9 mm is patched on the FR-4 substrate. The antenna is very large size and of very complicated structure than proposed antenna. The square patch of size 30 mm*30 mm with T-slot and defective ground structure is discussed in [5]. The antenna resonates at multi-frequency. The structure is simple but it does not provide better return loss than proposed antenna. In [6], the truncated circular patch of radius 40 mm is patched on the FR-4 substrate with double U slot. Air gap is introduced between the substrate and ground plane. Use of air gap may increases the size of the antenna. This air gap is avoided in the proposed antenna. In [7], the antenna of rectangular patch with size 23.4 mm*18.2 mm is patched on the substrate and two T-slots are made on this patch. The antenna is fed by microstrip feed. But this antenna uses two T-slots to produce multi frequency. In [8], the square spiral patch antenna with size 33.7 mm*33.7 mm is patched on the FR-4 substrate. The antenna is of very large size and complicated design as compared to proposed antenna.

The proposed antenna is an elliptical shape of semi major axis 21 mm and semi minor axis 18.18 mm with T-slot on the elliptical patch. The antenna is fed by coaxial feed. There is no air gap. FR-4 substrate of thickness 2 mm with dielectric constant 4.4 is chosen. The antenna structure is simple and provides better return loss.

IV. CONCLUSION

From the analysis, it is concluded that the proposed antenna resonates at three different frequencies. The frequencies are 1.57 GHz, 1.96 GHz and 3.4 GHz, which has S_{11} (dB) of -31.06, -19.83 and -21.76 respectively. The frequencies can cover applications such as GPS and LTE. Simulation and measurement results are presented for validation of the design and slight deviation is observed, which is below the tolerable limit of 5%. It

is due to substrate, connector losses and fabrication tolerances.

REFERENCES

[1] J. S. Dahele, K. F. Lee, and D. P. Wong, "Dual-frequency stacked annular- ring microstrip antenna," *IEEE Trans. Antennas Propagat*., vol. AP-35, no. 11, pp. 1281-1285, 1987.

[2] J. Wang, R. Fralich, C. Wu, and J. Litva, "Multifunctional aperture-coupled stacked antenna," *Electron. Lett*., vol. 26, no. 25, pp. 2067-2068, 1990.

[3] F. Croq and D. M. Pozar, "Multifrequency operation of microstrip antennas using aperture coupled parallel resonators," *IEEE Trans. Antennas Propagat.*, vol. 40, no. 11, pp. 1367-1374, 1992.

[4] S. Natarajamani, S. K. Behera, and R. K. Mishra, "Design of multi slotted and multfrequency patch antenna," *Applied Electromagnetic Conference*, Kolkata, 2009.

[5] S. De, P. Samaddar, S. Sarkar, S. Biswas, et al., "Compact high gain multi-frequency microstrip antenna," *International Journal of Soft Computing and Engineering*, vol. 2, no. 6, 2013.

[6] S. Murugan, E. Sathish Kumar, and V. Rajamani, "Design and analysis of double U slot loaded dual frequency microstrip antenna," *Progress In Electromagnetics Research C*, vol. 45, pp. 101-112, 2013.

[7] D. Ramya Keertana, M. V. S. D. N. N. Murthy, B. Yeswanth, et al., "A novel multi frequency rectangular microstrip antenna with dual T shaped slots for UWB applications," *IOSR Journal of Electronics and Communication Engineering*, vol. 9, no. 1, 2014.

[8] A. Ghosal, A. Majumdar, S. Kumar Das, A. Das, "Wideband and multi-frequency square spiral microstrip patch antenna," *International Journal of Innovative Research in Computer and Communication Engineering*, vol. 3, no. 2, 2015.

[9] S. Das, P. P. Sarkar, and S. K. Chowdhury, "Modified π-shaped slot loaded multi-frequency microstrip antenna," *Progress In Electromagnetics Research B*, vol. 64, pp. 103-117, 2015.

[10] J. A. Ansari, K. Kumari, A. Singh, and A. Mishra, "Ultra-wideband co-planer microstrip patch antenna for wireless applications," *Wireless Pers. Commun*., vol. 69, pp. 1365-1378, 2013.

[11] I. J. Bahl and P. Bhartia, *Broadband Microstrip Patch Antennas*. Dedham: Artech House, 1980.

[12] T. S. Bird, "Definition and the misuse of return loss," *IEEE Antenna Propagation Magazine*, vol. 51, no. 2, pp. 166-167, 2009.

[13] P. Sekra, S. Shekhawat, et al., "Design of circularly polarised truncated elliptical patch antenna with improved performance," *Indian Journal of Radio & Space Physics*, vol. 40, pp. 227-233, 2011.

APPLIED COMPUTATIONAL ELECTROMAGNETICS SOCIETY EXPRESS JOURNAL
http://aces-society.org

INFORMATION FOR AUTHORS

PUBLICATION CRITERIA

Each paper is required to manifest some relation to applied computational electromagnetics. **Papers may address general issues in applied computational electromagnetics, or they may focus on specific applications, techniques, codes, or computational issues.** While the following list is not exhaustive, each paper will generally relate to at least one of these areas:

1. **Code validation.** This is done using internal checks or experimental, analytical or other computational data. Measured data of potential utility to code validation efforts will also be considered for publication.

2. **Code performance analysis.** This usually involves identification of numerical accuracy or other limitations, solution convergence, numerical and physical modeling error, and parameter tradeoffs. However, it is also permissible to address issues such as ease-of-use, set-up time, run time, special outputs, or other special features.

3. **Computational studies of basic physics.** This involves using a code, algorithm, or computational technique to simulate reality in such a way that better, or new physical insight or understanding, is achieved.

4. **New computational techniques** or new applications for existing computational techniques or codes.

5. **"Tricks of the trade"** in selecting and applying codes and techniques.

6. **New codes, algorithms, code enhancement, and code fixes.** This category is self-explanatory, but includes significant changes to existing codes, such as applicability extensions, algorithm optimization, problem correction, limitation removal, or other performance improvement. **Note: Code (or algorithm) capability descriptions are not acceptable, unless they contain sufficient technical material to justify consideration.**

7. **Code input/output issues.** This normally involves innovations in input (such as input geometry standardization, automatic mesh generation, or computer-aided design) or in output (whether it be tabular, graphical, statistical, Fourier-transformed, or otherwise signal-processed). Material dealing with input/output database management, output interpretation, or other input/output issues will also be considered for publication.

8. **Computer hardware issues.** This is the category for analysis of hardware capabilities and limitations of various types of electromagnetics computational requirements. Vector and parallel computational techniques and implementation are of particular interest.

Applications of interest include, but are not limited to, antennas (and their electromagnetic environments), networks, static fields, radar cross section, inverse scattering, shielding, radiation hazards, biological effects, biomedical applications, electromagnetic pulse (EMP), electromagnetic interference (EMI), electromagnetic compatibility (EMC), power transmission, charge transport, dielectric, magnetic and nonlinear materials, microwave components, MEMS, RFID, and MMIC technologies, remote sensing and geometrical and physical optics, radar and communications systems, sensors, fiber optics, plasmas, particle accelerators, generators and motors, electromagnetic wave propagation, non-destructive evaluation, eddy currents, and inverse scattering.

Techniques of interest include but not limited to frequency-domain and time-domain techniques, integral equation and differential equation techniques, diffraction theories, physical and geometrical optics, method of moments, finite differences and finite element techniques, transmission line method, modal expansions, perturbation methods, and hybrid methods.

Where possible and appropriate, authors are required to provide statements of quantitative accuracy for measured and/or computed data. This issue is discussed in "Accuracy & Publication: Requiring, quantitative accuracy statements to accompany data," by E. K. Miller, ACES Newsletter, Vol. 9, No. 3, pp. 23-29, 1994, ISBN 1056-9170.

SUBMITTAL PROCEDURE

All submissions should be uploaded to ACES server through ACES web site (http://aces-society.org) by using the upload button, Express Journal section. Only pdf files are accepted for submission. The file size should not be larger than 6MB, otherwise permission from the Editor-in-Chief should be obtained first. Automated acknowledgment of the electronic submission, after the upload process is successfully completed, will be sent to the corresponding author only. It is the responsibility of the corresponding author to keep the remaining authors, if applicable, informed. Email submission is not accepted and will not be processed.

EDITORIAL REVIEW

In order to ensure an appropriate level of quality control, papers are peer reviewed. They are reviewed both for technical correctness and for adherence to the listed guidelines regarding information content and format.

PAPER FORMAT

Only camera-ready electronic files are accepted for publication. The term **"camera-ready" means that the material is neat, legible, reproducible, and in accordance with the final version format listed below.**

The following requirements are in effect for the final version of an ACES Express Journal paper:

1. The paper title should not be placed on a separate page. The title, author(s), abstract, and (space permitting) beginning of the paper itself should all be on the first page. The title, author(s), and author affiliations should be centered (center-justified) on the first page. The title should be of font size 14 and bolded, the author names should be of font size 12 and bolded, and the author affiliation should be of font size 10 (regular font, neither italic nor bolded).

2. An abstract is required. The abstract should be a brief summary of the work described in the paper. It should state the computer codes, computational techniques, and applications discussed in the paper (as applicable) and should otherwise be usable by technical abstracting and indexing services. The word "Abstract" has to be placed at the left margin of the paper, and should be bolded and italic. It also should be followed by a hyphen (–) with the main text of the abstract starting on the same line.

3. All section titles have to be centered and all the title letters should be written in caps. The section titles need to be numbered using roman numbering (I. II. ….)

4. Either British English or American English spellings may be used, provided that each word is spelled consistently throughout the paper.

5. Internal consistency of references format should be maintained. As a guideline for authors, we recommend that references be given using numerical numbering in the body of the paper (with numerical listing of all references at the end of the paper). The first letter of the authors' first name should be listed followed by a period, which in turn, followed by the authors' complete last name. Use a comma (,) to separate between the authors' names. Titles of papers or articles should be in quotation marks (" "), followed by the title of the journal, which should be in italic font. The journal volume (vol.), issue number (no.), page numbering (pp.), month and year of publication should come after the journal title in the sequence listed here.

6. Internal consistency shall also be maintained for other elements of style, such as equation numbering. Equation numbers should be placed in parentheses at the right column margin. All symbols in any equation have to be defined before the equation appears or right immediately following the equation.

7. The use of SI units is strongly encouraged. English units may be used as secondary units (in parentheses).

8. Figures and tables should be formatted appropriately (centered within the column, side-by-side, etc.) on the page such that the presented data appears close to and after it is being referenced in the text. When including figures and tables, all care should be taken so that they will appear appropriately when printed in black and white. For better visibility of paper on computer screen, it is good to make color figures with different line styles for figures with multiple curves. Color should also be tested to insure their ability to be distinguished after black and white printing. Avoid the use of large symbols with curves in a figure. It is always better to use different line styles such as solid, dotted, dashed, etc.

9. A figure caption should be located directly beneath the corresponding figure, and should be fully justified.

10. The intent and meaning of all text should be clear. For authors who are not masters of the English language, the ACES Editorial Staff will provide assistance with grammar (subject to clarity of intent and meaning). However, this may delay the scheduled publication date.

11. Unused space should be minimized. Sections and subsections should not normally begin on a new page.

ACES reserves the right to edit any uploaded material, however, this is not generally done. It is the author(s) responsibility to provide acceptable camera-ready files in pdf and MSWord formats. Incompatible or incomplete files will not be processed for publication, and authors will be requested to re-upload a revised acceptable version.

COPYRIGHTS AND RELEASES

Each primary author must execute the online copyright form and obtain a release from his/her organization vesting the copyright with ACES. Both the author(s) and affiliated organization(s) are allowed to use the copyrighted material freely for their own private purposes.

Permission is granted to quote short passages and reproduce figures and tables from an ACES Express Journal issue provided the source is cited. Copies of ACES Express Journal articles may be made in accordance with usage permitted by Sections 107 or 108 of the U.S. Copyright Law. The consent does not extend to other kinds of copying, such as for general distribution, for advertising or promotional purposes, for creating new collective works, or for resale. The reproduction of multiple copies and the use of articles or extracts for commercial purposes require the consent of the author and specific permission from ACES. Institutional members are allowed to copy any ACES Express Journal issue for their internal distribution only.

PUBLICATION CHARGES

There is a $200 basic publication charge assigned to each paper for ACES members, and $300 charge for non-ACES members. Corresponding authors should be active members of the society at the time of submission and the time of publication in order to receive the reduced charge.

ACES Express Journal doesn't allow for more than four pages. All authors must comply with the page limitations. ACES Express Journal is an online journal, and printed copies are not available.

Upon completion of its first year, ACES Express Journal will be abstracted in INSPEC, in Engineering Index, DTIC, Science Citation Index Expanded, the Research Alert, and to Current Contents/Engineering, Computing & Technology.